International Journal of Heat and Mass Transfer 53 (2010) 2662–2669

Contents lists available at ScienceDirect

International Journal of Heat and Mass Transfer

journal homepage: www.elsevier.com/locate/ijhmt

Multi-artery heat pipe spreader: Experiment

G.S. Hwang [a], Y. Nam [b], E. Fleming [c], P. Dussinger [c], Y.S. Ju [b], M. Kaviany [a,*]

[a] Department of Mechanical Engineering, University of Michigan, Ann Arbor, MI 48109, USA
[b] Mechanical and Aerospace Engineering Department, University of California, Los Angeles, CA 90095, USA
[c] Advanced Cooling Technologies, Inc., Lancaster, PA 17601, USA

ARTICLE INFO

Article history:
Received 15 September 2009
Received in revised form 27 January 2010
Accepted 27 January 2010
Available online 19 March 2010

Keywords:
Multi artery
Heat spreader
Meniscus recess
Capillary
Wick
Vapor chamber
Hysteresis

ABSTRACT

We constructed a low thermal resistance, multi-artery heat pipe spreader vapor chamber by designing a thin (monolayer) evaporator wick and distributed permeable columnar arteries supplying liquid (water) to highly concentrated heat source region. The condenser wick is layered copper screens in intimate contact with the columnar arteries. The vapor chamber is sealed and externally surface-convection cooled on the condenser side. For the evaporator wick and arteries, sintered, surface etched-oxidized copper particles are used to enhance wettability.

The measured evaporator thermal resistance is less than 0.05 K/(W/cm^2) using a 1 cm^2 heat source, and the critical heat flux is about 380 W/cm^2. This is in good agreement with thermal–hydraulic network models prediction, 389 W/cm^2. The resistance is dominated by the small effective thermal conductivity of the evaporator wick and by the small conduction path through the receding meniscus within it. This resistance decreases nonlinearly with the heat flux, due to a decrease in the radius of the receding meniscus.

1. Introduction

Heat pipes are widely used in the thermal management of high-performance electronic devices, as they offer simple, reliable and passive cooling solutions. However, conventional heat pipe performance deteriorates under high heat flux with concentrated heating, and its cylindrical geometry mismatches planar interface of semiconductor devices and packages. So, thin, planar heat pipes have been examined, mostly micro-fabricated silicon or metallic wick structures capable of heat fluxes below 200 W/cm^2 [1–3]. However, many new semiconductor devices (e.g., dense array power amplifiers for microwave and radio-frequency applications, power-conditioning and switching devices for electrical propulsion applications) dissipate heat fluxes greater than 250 W/cm^2 over areas of the order of 1 cm^2. This high flux heat removal is limited by the large thermal resistance of the liquid-filled evaporator wick (small effective thermal conductivity), unless it is made very thin. Thus, the optimal design requires an evaporator wick with strategic, distributed liquid supply, effective vapor removal, and a short conduction path.

Biporous wicks [4,5] and multi-artery wick [6,7] allow for such strategic liquid supply and vapor escape through high permeable wicks and a large evaporation area. Similarly, small thermal–hydraulic resistance has been used in the modulated-wick heat pipe [8] and in pool boiling [9] to enhance the critical heat flux (CHF). These enhancements are mainly limited by the fabrication challenges in the modulation pitch and the height-to-base aspect ratio, but fabrication advances continue to be made [10].

Here, we describe fabrication and testing of a multi-artery heat pipe spreader (MAHPS), and extend the analysis [6] to include our experimental observation of a receding meniscus inside the thin evaporator wick. This meniscus recession makes for an extremely low evaporator thermal resistance (which is many times larger in the uniform artery vapor chamber [11]) in the pre-CHF regime.

2. MAHPS construction

The multi-artery heat pipe spreader (MAHPS) is a vapor chamber using posts as liquid artery, as shown in Fig. 1. Heat and liquid/vapor flow paths, from heat source to the external heat sink, along with the evaporator, arteries, and condenser, are also shown. MAHPS has a thin evaporator wick and multilayer screen condenser wicks connected by the capillary arteries. The capillary arteries deliver liquid from the condenser to the evaporator wick due to smaller meniscus radius at the evaporation sites. Water is used as working fluid for high capillary pumping pressure (surface tension) and large heat of evaporation. Phase change occurs at the liquid–vapor interface on the evaporator and condenser wicks, and the generated vapor spreads and moves toward the condenser, where it is uniformly condensed over a large area. The condensed liquid returns towards the evaporator through the capillary suction.

* Corresponding author. Tel.: +1 734 936 0402; fax: +1 734 647 3170.
E-mail address: kaviany@umich.edu (M. Kaviany).

0017-9310/$ - see front matter © 2010 Published by Elsevier Ltd.
doi:10.1016/j.ijheatmasstransfer.2010.02.046

Nomenclature

A	(cross-section) area (m^2)
D	diameter (m)
d	(column) diameter (m)
F	constant
g	gravitational acceleration (m^2)
K	permeability (m^2)
k	thermal conductivity (W/m-K)
L	length (m)
p	pressure (Pa)
Q	heat flow rate (W)
q	heat flux (W/m^2)
R	resistance (K/W)
T	temperature (K)

Greek symbols

ϵ	porosity
δ	thickness (m)
μ	viscosity (Pa-s)
ρ	density (kg/m^3)
σ	surface tension (N/m)

Subscripts

a	apparent
c	capillary, column, condenser
e	evaporator
eff	effective
f	fluid
p	particle or pore
lg	liquid–gas phase change, or saturation
s	surface or solid
w	wick

Evaporator and artery wicks are fabricated by sintered copper powders, and then surface etched-oxidized for improved wetting. Small particles $d_{p,e} = 60$ μm are used in the evaporator for a low thermal resistance, whereas large particles, $d_{p,c} = 150$ μm are used in the posts for large permeability. The evaporator wick extends beyond the heater area, up to approximately 8 cm^2 [6]. No wick is used outside this area, so all liquid delivery is through the permeable arteries to the evaporator wick. An array of 12 arteries is used, and their diameter is optimized including the fabrication constraints [6]. The condenser wick is fabricated by two layers of 145 × 145 mesh copper screen, covering an entire area (Fig. 1). In addition, another two-layered strips of the same mesh screen in 1.9 cm width are used along the central line (rather than whole layers) to minimize the total amount of screen being used without hydraulically limiting the performance. The vapor chamber is made of two copper plates (CDA-101), welded after wick fabrication to form a sealed vapor space. The heater size is 1 × 1 cm^2, and the condenser size is 12 × 7 cm^2. Dominant heat transfers through the evaporator wick with small heat spreading, and this leads to evaporation mostly at the base of the arteries [6].

3. Experiment

3.1. Heat flow and wick superheat measurement

MAHPS is tested in a set up shown in Fig. 2, with Joule heating provided through a copper block with embedded four cartridges capable of up to 1 kW (controlled by a Variac). Heat then flows through a 1 cm^2 rectangular pedestal extending from MAHPS. Two thermocouples in the pedestal are used to determine the heat flow rate q with the Fourier law, and the evaporator surface temperature (beneath the evaporator wick, T_s) by extrapolation. The vapor (saturation) temperature T_{lg} is measured with a thermocouple spaced in the vapor space, and assuming thermal equilibrium. The wick superheat is $T_s - T_{lg}$.

MAHPS is insulated using Kaowool™ insulation. However, there are heat losses from the heater and heater–pedestal interface, causing measurement uncertainties both in the heat flow and wick superheat. An uncertainty analysis is performed by considering the precision uncertainty of the DAQ system (assumed negligible by averaging every 10 samples), the uncertainty in the thermocouples,

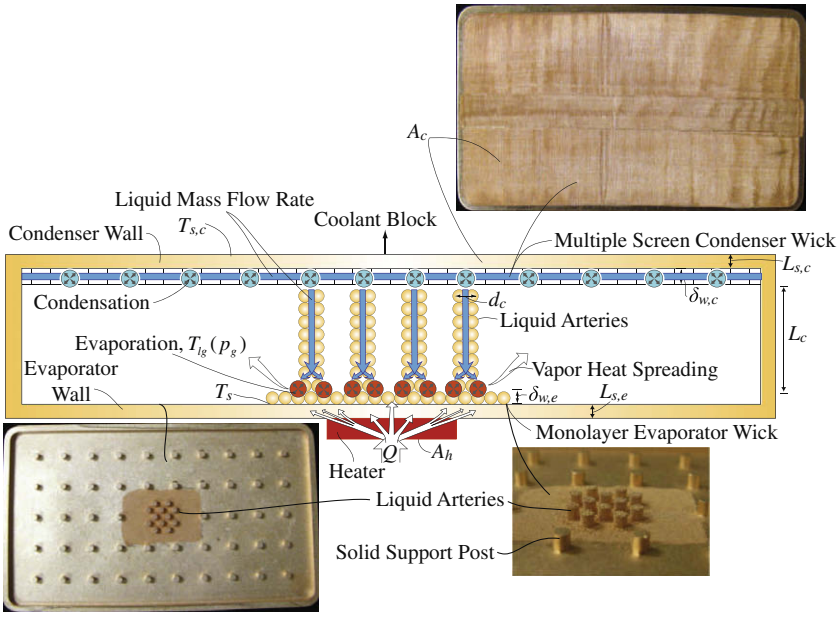

Fig. 1. A schematic of MAHPS. The thin evaporator wick, liquid arteries, multiple screen layer condenser wick (including central strips), are shown. Phase change, heat, liquid and vapor flow paths, and key dimensions are also illustrated. Images of monolayer evaporator wick, liquid artery posts, and screen condenser wick are also shown.

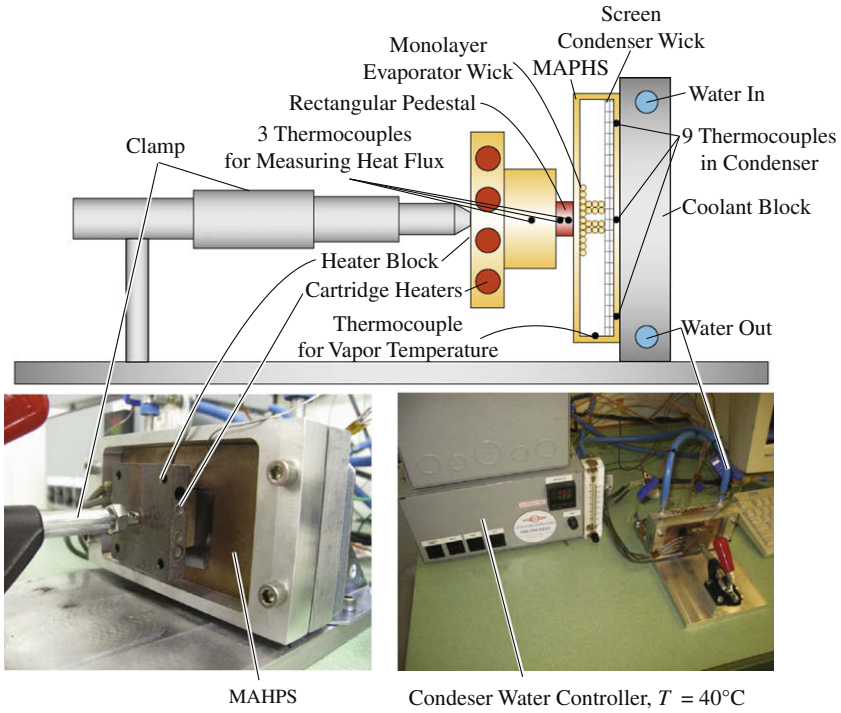

Fig. 2. A schematic drawing and image of the test section. The heater block, rectangular pedestal, MAHPS, condenser water cooler, and thermocouple placements are also shown.

±0.06 K (determined through constant temperature bath calibration), the distance measurement in caliper, 0.001 in, and the thermal conductivity of copper, ±0.5% [12]. These uncertainties are summed to attain a total bias uncertainty for q = 100 W, 200 W, and 400 W, varying from 0.8% to 1.7%. This uncertainty decreases with increasing flux, but even maximum values are too small to account for differences found amongst tests. Further investigation shows that the dominant source of uncertainty results from the clamping of the heater to MAHPS. From 10 individual tests at q = 100 W, the standard error, Δq_s, is found to be 3.3 W/cm^2 relative to the difference between the vapor and condenser temperatures. The corresponding bias uncertainty is then 6.6 W/cm^2, using the given relation [12]

$$\Delta q_e = F\Delta q_s, \tag{1}$$

where F is a constant, and F = 2 is used because we have 10 tests. This corresponds to an overall uncertainty in heat flux of ±9%. This uncertainty is also propagated through to the extrapolated evaporator temperature and eventually to the wick superheat. However, the resulting superheat uncertainty is neither constant in magnitude or percentage, varying from 2% to 6% for wick superheat ranging from 3 to 20 °C.

For heat removal, an aluminum water cooled block is mechanically fastened to the condenser side of the MAHPS with a graphite foil thermal interface. The cooling water is kept a constant flow rate of 12 gph and a constant inlet temperature of 40 °C throughout the test. The coolant flow rate is chosen to minimize calorimetry uncertainties and to allow for a nearly constant coolant temperature across the condenser, which is $\Delta T \sim 5$ °C at 250 W/cm^2. The condenser temperature is measured at six different locations. MAHPS is tested where the axial direction of the arteries is perpendicular to gravity vector (no gravity effect is expected due to the small Bond number).

3.2. Characterization of evaporator wick

Fig. 3(a) is a SEM micrograph of the monolayer, sintered non-oxidized copper powder evaporator wick. The wick effective thermal conductivity is predicted $\langle k_{w,e}\rangle$ using a relation for bulk porous media [13]

$$\langle k_{w,e}\rangle = k_f\left(\frac{k_s}{k_f}\right)^{0.280-0.757\log(\epsilon_{w,e})-0.057(k_s/k_f)}, \tag{2}$$

where $\epsilon_{w,e}$ is the porosity of wick, k_f and k_s are the thermal conductivities of water and copper. Since we have a monolayer, we also use a relation for the half-diameter region adjacent to planar surface [14]

$$\frac{\langle k_{w,e}\rangle}{k_f} = \epsilon_{w,e} + \frac{1-\epsilon_{w,e}}{2\phi_w + \frac{2}{3}\frac{k_f}{k_s}}. \tag{3}$$

Using Eqs. (2) and (3), $\langle k_{w,e}\rangle$ = 10 and 4.6 W/m-K, assuming $\epsilon_{w,e}$ = 0.4. We expect the effective thermal conductivity of the monolayer to be between these two and use $\langle k_{w,e}\rangle$ = 6 W/m-K.

The wick permeability K is measured using the liquid rising rate caused by capillary suction [15,16]. The relation is [15,16]

$$z\frac{dz}{dt} = \frac{K}{\epsilon_{w,e}\mu_l}\left(\frac{2\sigma}{r_{c,min}} - \rho g z\right), \quad r_c = \frac{r_p}{\cos\theta_c}, \tag{4}$$

where K is the permeability, $\epsilon_{w,e}$ is the porosity of the evaporator wick, and $r_{c,min}$ is the effective capillary meniscus determined by the pore radius r_p and the contact angle of the wick surface θ_c, and z and μ_l are the rising height and the viscosity of the liquid.

Wicks (1 cm × 5 cm) are placed along the gravity vector above a liquid pool. The upper part of the wick is held by a sample holder connected to the z-stage. The wick is slowly lowered using the z-stage and upon touching the reservoir the liquid rises quickly. Methanol is used as the test liquid. The contact angle of water on unoxidized Cu surfaces is too large to achieve spontaneous

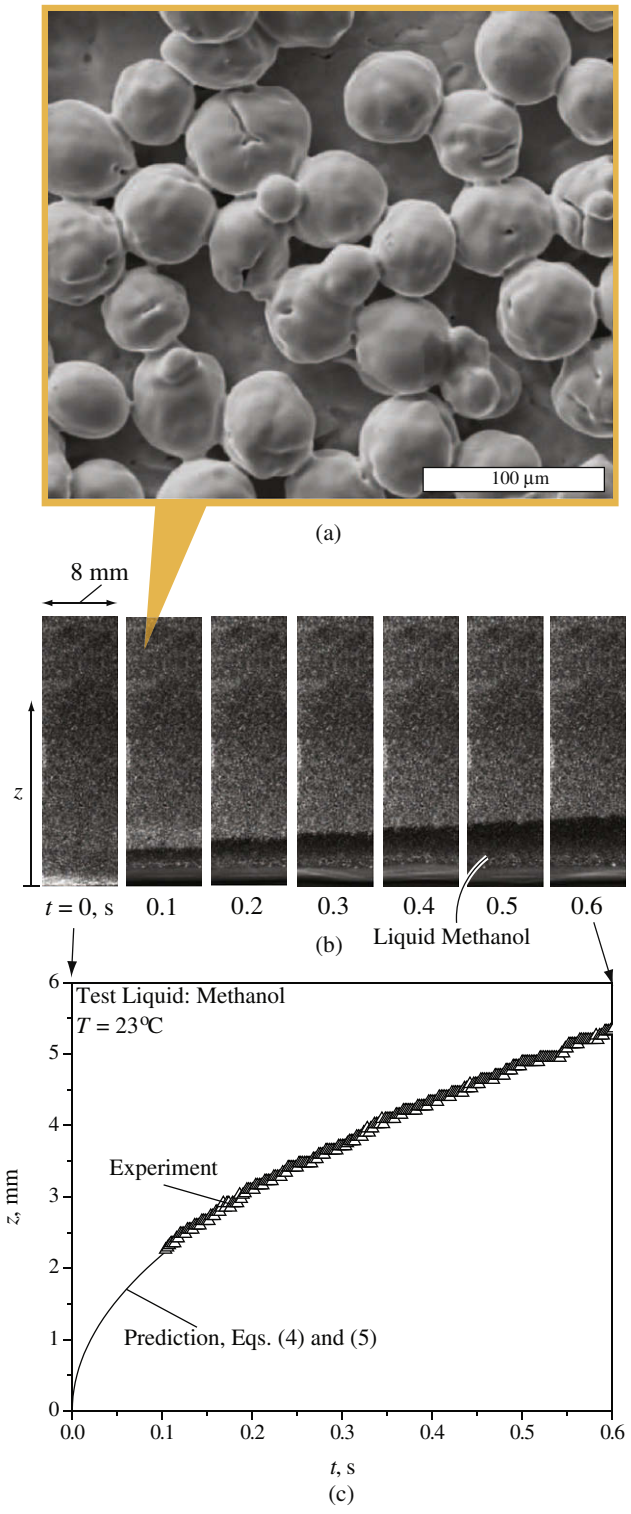

Fig. 3. (a) SEM micrograph of monolayer, sintered, non-oxidized copper powder evaporator wick (on copper substrate), showing large void spaces. The liquid initially floods the wick, and as the heat flux increases, the meniscus recedes. (b) Snap shots of liquid methanol rising through an evaporator wick, front view. The width of each image is 8 mm. (c) Measured liquid rise height as a function of time, and comparison with the best fit using Eqs. (4) and (5).

capillary rise. Methanol wets both unoxidized and oxidized copper surfaces very well and provides acceptable optical contrast between dry and wet regions. We note that the capillary rate of rise experiment was conducted to characterize permeability (K) and pore radius (r_p). Both factors are determined by the wick geometry, and the choice of test liquid does not affect the final results. For ease of visualization (contrast between dry and wet regions), 0.1% (by weight) Fluorescein is premixed with the methanol, and the wick surface is illuminated using a LED lamp (Philips Luxeon 3). Upon the bottom tip of the wick touching the liquid surface, the rise of the three-phase contact line (transient capillary height) is recorded using a high speed camera (Fastcam MC2, Photron) with 500 fps. The light intensity distribution is also measured to quantify the rising height. The recorded height-time data are curve fitted using Eq. (4), and the magnitude of K/r_c is obtained from the best fit which minimizes the mean absolute deviation (M.A.D., average value of $(t_m - t_c)/t_c \times 100(\%)$, t_m is the measured value, and t_c is the calculated value). We also use porosity $\epsilon_{w,e} = 0.5$ [image analysis from Fig. 3(a)]. The methanol properties at $T = 23$ °C are used [17], as summarized in Tables 1 and 2.

Fig. 3(b) shows snap shots for the rising liquid. Due to the small contact angle of methanol, liquid rises quickly through the wick. The contact line shows some fingering, because of the heterogeneities in the wick. The reflected light intensity distribution is averaged along the width of the wick to minimize the effect of this nonuniformity. Initially, a macroscopic meniscus forms at the tip of the wick, and the maximum height of the meniscus is estimated as 2.4 mm, using the following relation [18]

$$z_{max} = \left(\frac{2\sigma}{\rho g}\right)^{1/2} (1 - \sin\theta_a)^{1/2}, \tag{5}$$

where θ_a represents the apparent contact angle. In order to separate this tip wetting effect from the internal wicking, the maximum height of the meniscus is subtracted from the data (with the associated time), and then fitted while removing the initial 100 ms data, to minimize the dynamic effect caused by the macroscopic meniscus formation.

Fig. 3(c) shows the measured rising height as a function of the time, and also compares with the discussed best fit. The sampling rate is 500 fps. The magnitude of M.A.D. is 3%. Each measurement is repeated three times, and the average value of $K/r_{c,min}$ is measured as 1.56×10^{-7} m with 2.52×10^{-9} m standard deviation. Since the monolayer wick has a free surface with a measured, zero contact angle, we use the particle radius as the effective capillary meniscus [19], i.e., $r_{c,min} = r_p$ where $r_p = 30$ µm. As a result, we have $K = 4.68 \times 10^{-12}$ m^2. This value is used for the network model [6].

3.3. Oxidization of evaporator wick

Copper is a choice wick material for its high thermal conductivity and favorable processing properties. At moderate temperatures, water is the liquid choice of its low cost, ease of handling and high figure of merit [8]. However, poor wettability of water-copper ($\theta_a \approx 90^\circ$) hinders high performance and should be remedied.

We apply a thermal oxidation process to enhance wetting of the evaporator copper wick. Oxidizing a copper surface is a convenient way to enhance the wetting by changing both the surface energy and roughness. During the thermal oxidation process, a Cu_2O layer first forms on the copper surface, and when this Cu_2O layer reaches

Table 1
Methanol properties for capillary rise in the evaporator wick, at $T = 23$ °C [17].

Parameter	Quantity	Magnitude
ρ	Density	788.1 kg/m^3
σ	Surface tension	22.43 mN/m
μ_l	Viscosity	5.706×10^{-4} Pa-s
θ_c	Contact angle	<5°
θ_a	Apparent contact angle	≈0°

Table 2
Geometric parameters for MAHPS design.

Parameter	Quantity	Magnitude
A_h	Heater area	1×1 cm^2
A_c	Condenser area	12×7 cm^2
L_c	Column height	2.6 mm
L_p	Pitch of arteries	3.52 mm
$L_{s,e}$	Evaporator wall thickness	1 mm
$L_{s,c}$	Condenser wall thickness	1 mm
$d_{p,e}$	Evaporator wick particle diameter	60 μm
$\delta_{w,e}$	Evaporator wick thickness (flooded)	60 μm
d_c	Column diameter	2.2 mm
m_l	Fluid charge mass	2.55 g

a critical thickness of about 90–300 nm [20], a CuO layer begins to grow. It has been reported that the CuO layer grows only at the elevated temperature of about 260 °C [20].

Investigation of the effect of temperature (150–250 °C) on the wettability and the morphology of a copper surface has shown that higher temperatures induce larger wettability enhancement and higher roughness factor [21]. However, the oxide layer grown at high temperatures tends to peel off, because of induced thermal stress [21]. We thermally oxidize a sintered copper powder at 150 °C to avoid this thermal stress problem. To enhance the oxidation rate, the oxidation is conducted under wet condition [22]. First, we fully saturate the wick with water, and then heat to 150 °C in an oven, until the wick is completely dry. The wick is continuously heated at 150 °C for 1 h and saturated with water every 5 min. The saturation-drying cycle is repeated 12 times.

Fig. 4(a) and (b) show SEM micrographs of a copper particle in the evaporator wick before and after oxidation. Magnified images are also shown in the insets. Fig. 4(c) and (d) also show water droplets placed on the wick surfaces. The apparent contact angle on the wick surface is measured using a droplet (4 μl) of water placed on the wick and then image of droplet is recorded and analyzed using a goniometer (First Ten Angstroms, FTA 4000A). Because of the nonuniform distribution of sintered copper powder, the contact angle is measured at 10 different locations and the averaged value is used with the standard deviation. Before the oxidation, water does not wet the wick well and the apparent contact angle was measured to be $93.9 \pm 5.8°$. After this oxidation, the contact angle decreases to $42.8 \pm 5.7°$, however, in general oxidation results in even better wetting. So, this contact angle is larger than in the permeability experiments (near ideal wetting with methanol in Section 3.2). It should be noted that wetting may improve in the geometrically confined pores, and these overlapping surface forces results in more hydrophilic-like wetting. Thus, we assume ideal wetting in our modeling (Section 4).

In general, wetting is enhanced by increases both in surface energy and surface roughness. However, we believe that the increase in surface roughness is not the primary cause of the improved wetting. The effective contact angle θ_a by surface roughness given by [23]

$$\cos\theta_a = f_r \cos\theta_s, \tag{6}$$

where θ_s is the contact angle of a smooth surface, and f_r is a roughness factor ($f_r = A_r/A_g$, A_r is real surface area and A_g is smoothed surface area). In our individual contact angle test [21], the measured contact angle of air-exposed smooth copper substrate is $\theta_s \sim 85°$, and even with 50% increase in the roughness factor ($f_r = 1.5$), the predicted apparent contact angle change is negligibly small, $\theta_a \sim 82.5°$. This implies that the significant increase in surface wettability results from the increase in surface energy, and not the increase in the surface area.

Indeed, a thermal oxidation process creates a thin, oxidized layer on the wick surface, which in turn increases a thermal resistance. However, the overall increase is expected to be small because of its thin layer, 0.2 μm. This oxidize layer also improves wetting, which in turn enhances CHF by increasing capillary pressure. Our

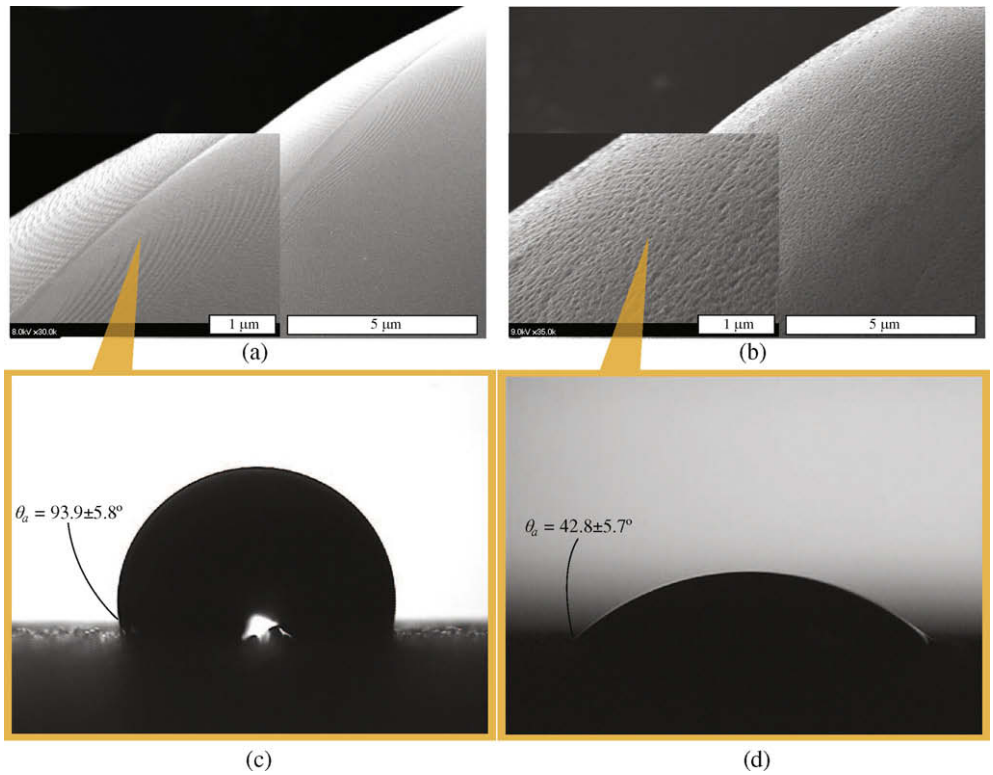

Fig. 4. A droplet (4 μl) of water placed on a sintered copper powder wick, (a) before ($\theta_a = 93.9 \pm 5.8°$), and (b) after oxidation ($\theta_a = 42.8 \pm 5.7°$). SEM micrographs of a sintered copper particle, as a part of the evaporator wick, (c) before, and (d) after oxidation. Magnified images are also shown in insets.

experimental results show that this benefit of thin oxide layers surpasses its small parasitic thermal resistance.

4. Results and discussion

Fig. 5(a) shows experimental results for variations of the heat flux q (up to the critical heat flux q_{CHF}) with respect to the evaporator wick superheat $T_s - T_{lg}$. It should be noted that a full liquid (water) charge (fully-flooded wicks) was used. The theoretical ideal charge is complete wick saturation without excess liquid. If the total volume of liquid is less than the wick void volume, CHF will not be maximized due to insufficient liquid supply to the evaporator. If significant excess liquid exists, effective condenser area is reduced, resulting in a larger condenser resistance and testing has also shown adverse effects on evaporator resistance. To ensure optimal liquid charge, the total void volume was estimated based on wick porosity, and the MAHPS is initially charged with 120% of this liquid volume. The MAHPS is tested at 4 different charges to identify the minimum liquid charge, which did not reduce the CHF. This charge, 2.55 g, is used for all experimental results presented throughout this paper. The experiments were repeated three times for repeatability, and only one set of data is shown for clarity. The wick superheat increases almost linearly with heat flux up to $q = 150$ W/cm^2, and then nonlinearly up to 250 W/cm^2, i.e., a decrease in thermal resistance. As q further increases, the wick superheat remains constant (or decreases) up to $q = 350$ W/cm^2, and then increases till dryout $q_{CHF,e} = 387$ W/m^2. A decrease in the superheat with an increase in heat flux is also observed in a looped heat pipe using a biporous wick [4]. As discussed below, CHF is due to the hydraulic limit (capillary-viscous chocking), as compared to the wick superheat limit (bubble forming inside the wick). For the hydraulic limit, we predict $q_{CHF,p}$ using the network model [6] and the Darcy relation [19]

$$p_{c,max} \geqslant \frac{\mu_l \dot{M}_l}{\rho l A_{w,e} K} L_e, \quad \text{where } \dot{M}_l = \dot{M}_{lg} = \frac{Q}{\Delta h_{lg}}, \tag{7}$$

where $p_{c,max}$ is the maximum capillary suction pressure, μ_l is the liquid viscosity, L_e is the flow path length, $\dot{M}_l$ is the liquid mass flow rate, ρ_l is the liquid density, $A_{w,e}$ is the wick cross-sectional area, K is the monolayer wick permeability, $\dot{M}_{lg}$ is the evaporation rate, Q is the heat transfer rate, Δh_{lg} is the enthalpy of vaporization.In the hydraulic limit, the liquid pressure drop reaches the maximum capillary pressure.CHF is expected to occur when the base of the central liquid arteries dries out due to the largest hydraulic resistance.Although q_{CHF} depends on the hydraulic resistance of condenser, arteries, evaporator wick, the evaporator wick dominates, $R_{l,e}/R_{l,t} = 0.8$ due to small permeability and cross-section ($R_{l,a}/R_{l,t} = 0.05$ and $R_{l,c}/R_{l,t} = 0.15$) where $R_{l,e}, R_{l,a}, R_{l,c}$ are the resistance in the evaporator, artery, condenser wicks, respectively.$R_{l,t}$ is the total resistance of the central liquid artery ($R_{l,t} = R_{l,e} + R_{l,a} + R_{l,c}$).For the wick cross-sectional area $A_{w,e}$, the wick thickness $\langle \delta_{w,e} \rangle = 18$ μm [assumed, effective wick thickness when considering meniscus receding at high heat fluxes prior to CHF, Fig.5(b)] is used to predict CHF. The model predicts $q_{CHF,p} = 389$ W/cm^2, and shows good agreement with the experimental result of 387 W/cm^2.Here, this suggests that the hydraulic limit is reached first prior to the wick superheat limit due to no significant hydraulic transition behavior in the experimental data.As a reference, we also show the plain-surface pool boiling CHF, q_{CHF}[13], and this notes that the arteries are much more effective than the liquid–vapor counter flow of pool boiling. This is because the arteries effectively separate the liquid and vapor phases, and allow for strategic, local liquid delivery.

The measured evaporator thermal resistances $A_h R_{k,e}$, defined as $d\Delta T/dq$ here [as indicated in Fig. 5(a)], vary with the heat flux. This is due to the receding meniscus in the evaporator wick, represented by a heat flux-dependent effective wick thickness $\langle \delta_{w,e}(q) \rangle$. The proposed three regimes, related to the meniscus recesses, are shown in Fig. 5(b), starting with the flooded wick for $q = 0$. At the hydraulic limit $q_{CHF,p}$, the effective wick thickness reaches a minimum value where the contact line recedes and its radius decreases. These combined mechanisms are proposed for a nonlinear decrease in the wick thickness, with increasing q, and here for simplicity we use a quadratic relation

$$A_h R_{k,e} = \frac{\langle \delta_{w,e}(q) \rangle}{\langle k_{w,e} \rangle}, \quad \text{where } \langle \delta_{w,e}(q) \rangle = \delta_{w,e}(q=0) - \alpha q^2, \tag{8}$$

where $\delta_{w,e}(q = 0)$ is the flooded-wick thickness and α is the constant. It should be noted that Eq. (8) is oversimplified, and a fourth-order fit is more suitable (because it is necessary to consider

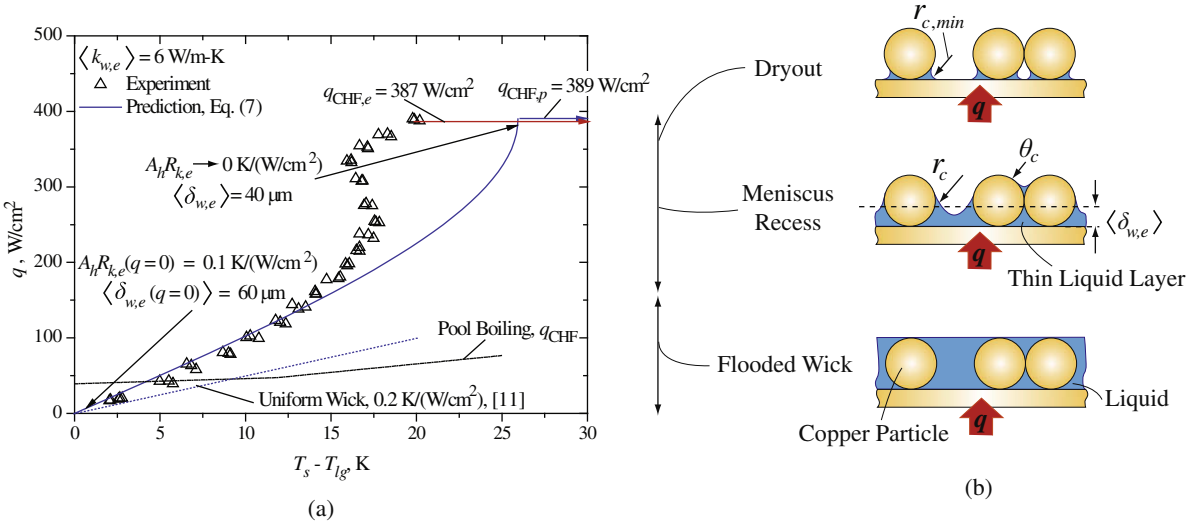

Fig. 5. (a) Variations of measured heat flux q up to the critical heat flux $q_{CHF,p}$, as a function of the evaporator wick superheat $T_s - T_{lg}$ using a full liquid charge. The predicted q_{CHF} using the network model [6], and temperature-dependant pool boiling q_{CHF} [13] are also shown. Prediction using the heat flux-dependent wick thermal resistances $A_h R_{k,e}$, and the wick thicknesses $\langle \delta_{w,e} \rangle$ at $q_{CHF,e}$ is shown. The wick thermal resistance of the uniform wick [11] is also shown. (b) Physical models of the meniscus (contact line) receding into the wick, showing flooded, receding, and dryout regimes. The contact angle is nearly zero for treated copper particle-water, and the meniscus radius of curvature r_c is also shown.

nonlinear recesses along with the complex meniscus morphologies on the particle surfaces). This study is left for future. Using this heat flux-dependent average meniscus location (and assuming local thermal equilibrium which is not easily justifiable), the relation between heat flux and wick superheat is

$$q = \frac{\langle k_{w,e} \rangle}{\delta_{w,e}(q=0) - \alpha q^2}(T_s - T_{lg}). \quad (9)$$

The value of $\alpha = 1.322 \times 10^{-8}$ cm/W^2 fits the experimental data at the low heat flux and results in $q_{CHF,p}$ predicted CHF with a zero thermal resistance (dryout) as shown in Fig. 5(a). For q = 0, this wick is flooded and the thermal resistance is predicted as $A_h R_{k,e} = 0.1$ K/(W/cm^2) for $\langle \delta_{w,e} \rangle = 60$ μm (one particle diameter), whereas it is close to 0 K/(W/cm^2) at CHF. Assuming no significant change in the effective evaporation area and wick thermal conductivity, it corresponds to $\langle \delta_{w,e} \rangle = 40$ μm using Eq. (8). This is reasonable considering that: (a) for an ideal wetting (contact angle of zero), and (b) meniscus recesses to $r_{c,min}$, where is $r_{c,min} = 0.41 r_p = 24$ μm [19].

This variable evaporator resistance predicts the experimental trend relatively well. However, it does not predict the decrease in the superheat prior to CHF. This is due to the lack of detailed mechanics and heat transfer of meniscus relocation inside the wick. To account for the moving (receding) meniscus in a heterogeneous wick requires a more detailed model of the meniscus-solid (including stochastic features of the pore distribution and presence of thermal non-equilibrium among phases) than given here.

The variation of the evaporator wick with an increase in heat flux results in significant changes in meniscus topologies, once the meniscus drops below the line passing through the particle centers. This can explain the reduction in the superheat at high heat flux. We have not yet thoroughly analyzed this, and instead have used the simplified effective wick thickness given by Eq. (8).

Fig. 6 shows effects of the heat flux increase/decrease increment in experiments Δq, as well as hysteresis, using the full liquid charge. The data for $\Delta q = 50$ W/cm^2 (increasing branch) shows a nonlinear increase in the wick superheat up to CHF, $q_{CHF,e} = 344$ W/cm^2. It is repeated using $\Delta q = 25$ W/cm^2 (increasing branch), showing similar results to $\Delta q = 50$ W/cm^2. The data for $\Delta q = -25$ W/cm^2 also shows no hysteresis. These suggest no bubble formation within the wicks and arteries at high heat fluxes (in pool boiling, trapped bubbles cause hysteresis [24]), so we suggest that the observed CHF is controlled by the hydraulic chocking. The average of three experiments, $q_{CHF,e} = 387$ W/cm^2 with $\Delta q = +25$ W/cm^2 is marked in Fig. 6.

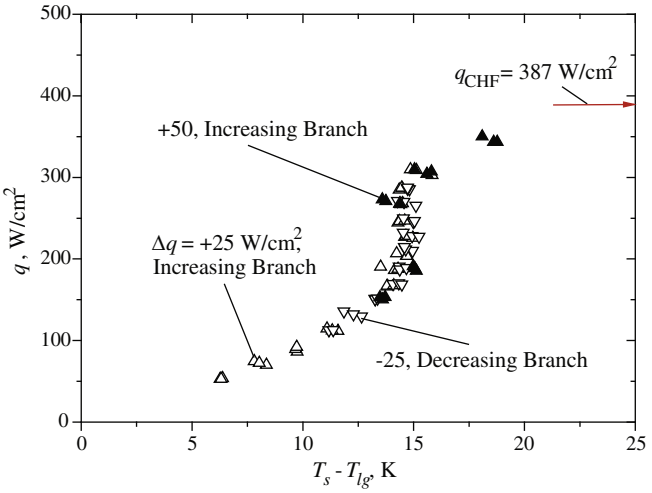

Fig. 6. Variations of measured heat flux q up to the critical heat flux $q_{CHF,p}$, as a function of the evaporator wick superheat $T_s - T_{lg}$ using a full liquid charge and heat flux increment $\Delta q = 25$ and 50 W/cm^2. For $\Delta q = 25$ W/cm^2, both increasing and decreasing branches for hysteresis test are also shown. The marked q_{CHF} is from Fig. 5.

5. Conclusions

We fabricate and test a MAHPS, focusing on small thermal resistance in a thin (monolayer) evaporator wick and low hydraulic resistance in the distributed liquid arteries and the evaporator wick. We find a hydraulic-limit CHF of about 380 W/cm^2. The evaporator wick resistance is the smallest at high heat fluxes and reaches about $A_h R_{w,e} \simeq 0.05$ K/(W/cm^2). This is much better (smaller thermal resistance and higher CHF) than the uniform artery heat spreader. We explain the low thermal resistance using a heat flux-dependent meniscus recess model (quadratic relation). We find no significant hysteresis.

Acknowledgements

This material is based upon work supported by the Defense Advanced Research Project Agency (DARPA) and Space and Naval Warfare Systems Center (SPAWARS-YSCEN), San Diego, CA under Contract No. N66001-08-C-2007. We are thankful for useful discussions on the network model with Da-Hye Min, currently a Ph.D. student at the University of Illinois-Urbana/Champaign. The findings contained in this article are those of the authors and should not be interpreted as representing the official views or policies, either expressed or implied, of the DARPA or the Department of Defense.

References

[1] M. Le Berre, G. Pandraud, P. Morfouli, M. Lallemand, The performance of micro-heat pipes measured by integrated sensors, J. Micromech. Microeng. 16 (2006) 1047–1050.
[2] R. Boukhanouf, A. Haddad, M. North, C. Buffone, Experimental investigation of a flat plate heat pipe performance using IR thermal imaging camera, Appl. Therm. Eng. 26 (2006) 2148–2156.
[3] C. Sobhan, R. Rag, G. Peterson, A review and comparative study of the investigations on micro-heat pipes, Int. J. Energy Res. 31 (2007) 664–688.
[4] C.-C. Yeh, C.-N. Chen, Y.-M. Chen, Heat transfer analysis of a loop heat pipe with biporous wicks, Int. J. Heat Mass Transfer 52 (2009) 4426–4434.
[5] T. Semenic, I. Catton, Experimental study of biporous wicks for high heat flux applications, Int. J. Heat Mass Transfer 52 (2009) 5113–5121.
[6] D.H. Min, G.S. Hwang, M. Kaviany, Multi-artery, heat pipe spreader, Int. J. Heat Mass Transfer 52 (2009) 629–635.
[7] S. Hsieh, R. Lee, J. Shyu, S. Chen, Analytical solution of thermal resistance of vapor chamber heat sink with and without pillar, Energy Convers. Manage. 48 (2007) 2708–2717.
[8] G.S. Hwang, M. Kaviany, W. Anderson, J. Zuo, Modulated wick heat pipe, Int. J. Heat Mass Transfer 50 (2007) 1420–1434.
[9] S. Liter, M. Kaviany, Pool-boiling CHF enhancement by modulated porous-layer coating: theory and experiment, Int. J. Heat Mass Transfer 44 (2001) 4287–4311.
[10] D.H. Min, G.S. Hwang, Y. Usta, O. Cora, M. Koc, M. Kaviany, 2-D and 3-D modulated porous coatings for enhanced pool boiling, Int. J. Heat Mass Transfer 52 (2009) 2607–2613.
[11] D. Mehl, P. Dussinger, K. Grubb, Use of vapor chambers for thermal management, in: National Electronic Packaging and Production Conference Proceedings of the Technical Program (East and West), vol. 3, 1999, pp. 1358–1366.
[12] A. Mills, B. Chang, Error analysis of experiments: a manual for engineering students, 2003, unpublished.
[13] M. Kaviany, Principles of Heat Transfer, Wiley, New York, 2002.
[14] K. Ofuchi, D. Kunii, Heat-transfer characteristics of packed beds with stagnant fluid, Int. J. Heat Mass Transfer 8 (1965) 749–757.
[15] B. Holley, A. Faghri, Permeability and effective pore radius measurements for heat pipe and fuel cell applications, Appl. Therm. Eng. 26 (2006) 448–462.
[16] N. Fries, K. Odic, M. Conrath, M. Dreyer, The effect of evaporation on the wicking of liquids into a metallic weave, J. Colloid Interface Sci. 321 (2008) 118–129.

[17] P. Linstrom, W. Mallard (Eds.), NIST Chemistry WebBook, NIST Standard Reference Database Number 69, National Institute of Standards and Technology, Gaithersburg, MD 20899, USA, 2009.
[18] P.-G. Gennes, F. Brochard-Wyart, D. Quéré, Capillarity and Wetting Phenomena: Drops, Bubbles, Pearls, Waves, Springer, New York, 2004.
[19] G. Peterson, An Introduction to Heat Pipes: Modeling, Testing, and Applications, Wiley, New York, 1994.
[20] F. Young, J. Cathcart, A. Gwathmey, The rates of oxidation of several faces of a single crystal of copper as determined with elliptically polarized light, Acta Metall. 4 (1956) 145–152.
[21] Y. Nam, Y.S. Ju, Comparative study of copper oxidation schemes and their effects on surface wettability, in: Proceedings of IMECE 2008, vol. 2008-67492, Boston, 2008, p. 273.
[22] R. Haugsrud, The influence of water vapor on the oxidation of copper at intermediate temperatures, J. Electrochem. Soc. 149 (2002) B14–B21.
[23] R. Wenzel, Resistance of solid surfaces to wetting by water, Ind. Eng. Chem. 28 (1936) 988–994.
[24] G.S. Hwang, M. Kaviany, Critical heat flux in thin, uniform particle coatings, Int. J. Heat Mass Transfer 49 (2006) 844–849.